INTERNATIONAL JOURNAL FOR NUMERICAL METHODS IN FLUIDS, VOL. 15, 59–82 (1992)

THE SIMULATION OF INVISCID, COMPRESSIBLE FLOWS USING AN UPWIND KINETIC METHOD ON UNSTRUCTURED GRIDS

J. S. MATHUR* AND N. P. WEATHERILL

Institute for Numerical Methods in Engineering, Department of Civil Engineering, University College of Swansea,
Singleton Park, Swansea SA2 8PP, U.K.

SUMMARY

A kinetic flux-vector-splitting method has been used to solve the Euler equations for inviscid, compressible flow on unstructured grids. This method is derived from the Boltzmann equation and is an upwind, cell-centred, finite volume scheme with an explicit time-stepping procedure. The Delaunay triangulation has been used to generate the grids. The approach is demonstrated for three flow field simulations, namely the subsonic flow over a two-component high-lift aerofoil, the transonic flow over an aerofoil and the supersonic flow in a channel.

KEY WORDS Inviscid compressible flow Upwind algorithm Cell centred Finite volume Unstructured grids

1. INTRODUCTION

Computational fluid dynamics applied to aeronautical flows has now progressed to a stage where the routine simulation of compressible, inviscid flow, represented by the Euler equations, is commonplace. The simulation procedure involves the discretization of the flow domain into a grid which consists of nodes and elements (cells) and this is then used for the numerical approximation of the governing flow equations. Different approaches to grid generation have been adopted. Structured grids can be generated by mapping techniques using algebraic interpolation[1] or the solution of partial differential equations.[2] For complicated geometries such techniques are applied in a multiblock decomposition of the flow domain.[3] Unstructured grids, traditionally used with the finite element method, are very flexible for use with complicated geometries and have been shown to be highly effective for mesh adaptivity. The advancing front technique[4] and the Delaunay triangulation[5] are two approaches which are now widely used.

The numerical algorithms developed to solve the flow equations are diverse. Much effort has been expended in developing algorithms to solve partial differential equations of elliptic or parabolic type.

However, the equations describing compressible flow problems are mainly of hyperbolic nature. For such equations discontinuities in boundary conditions are propagated as discontinuities into the solution domain and discontinuities in the solution can appear even when

---

* On leave from Computational and Theoretical Fluid Dynamics Division, National Aeronautical Laboratory, Bangalore, India.

0271-2091/92/130059-24$17.00

Received April 1991
Revised November 1991

smooth boundary data are imposed. In such cases the solution at any point depends on only some of the data in the flow domain and is independent of the rest. Several highly successful algorithms have been developed to solve such problems.[5-7]

One approach which has proved popular is the class of upwind methods. The strength of the upwind approach is its capacity to treat the discontinuities in the flow field and its ability to simulate directly the physics of the directional propagation of information. Examples of some of the commonly adopted approaches are the flux difference splitting of Roe[8,9] and Osher[10] and the flux vector splitting of Steger and Warming[11] and Van Leer.[12] Traditionally, such techniques have been applied on structured grids, where it is relatively easy to construct the operators required for the directional bias within the formulation.

Recently, some attention has been given to the construction of upwind flow algorithms on unstructured meshes.[13,14] Such an approach offers to combine the flexibility of unstructured meshes with the accuracy of upwind techniques. In this paper an upwind kinetic flux-vector-splitting (KFVS) technique is developed for use with unstructured grids. The approach is based upon the fact that the Euler equations of motion are the moments of the Boltzmann equation whenever the velocity distribution function is Maxwellian. The KFVS method is explicit, conservative, satisfies entropy conditions and has been combined with total-variation-diminishing (TVD) and UNO formulations to yield accurate solutions. To demonstrate the algorithm, it has been combined with an unstructured grid generator based upon the Delaunay triangulation to simulate the subsonic flow over a two-component aerofoil, the transonic flow over an aerofoil and the supersonic flow in a channel. Mesh adaptivity is applied to improve the flow field resolution.

2. THE KINETIC FLUX-VECTOR-SPLITTING METHOD

2.1. Basic concepts

The kinetic flux-vector-splitting (KFVS) method of Mandal and Deshpande[15-18] is an upwind method for the solution of inviscid, compressible, gasdynamic problems. It is based on the fact that the Euler equations of fluid mechanics can be obtained by taking moments of the Boltzmann equation with a Maxwellian velocity distribution function.[15,19-21]

The Boltzmann equation comes from the kinetic theory of gases and is given by

$$\frac{\partial f}{\partial t}+\mathbf{v}\cdot\frac{\partial f}{\partial \mathbf{x}}=J, \tag{1}$$

where f is the velocity distribution function which gives the number density in phase space of molecules with position $\mathbf{x}$ and velocity $\mathbf{v}$ at time t. The right-hand side of the equation represents a collision term which vanishes in the Euler limit. The Maxwellian distribution in two dimensions is given by

$$F=\frac{\rho}{I_0}\frac{\beta}{\pi}\exp\left(-\beta(v_1-u_1)^2-\beta(v_2-u_2)^2-\frac{I}{I_0}\right), \tag{2}$$

where $\beta=1/2RT$, ρ is the mass density, T is the temperature, R is the gas constant per unit mass, $\mathbf{v}=(v_1, v_2)^{\mathrm{T}}$ is the molecular velocity vector, $\mathbf{u}=(u_1, u_2)^{\mathrm{T}}$ is the fluid velocity vector, I is the internal energy variable corresponding to non-translational degrees of freedom (needed to force the given value of γ for the gas consisting of pseudo-particles), $I_0=[(2-\gamma)/(\gamma-1)]RT$ is the internal energy due to non-translational degrees of freedom and γ is the ratio of specific heats. The moment vector $\mathbf{\Psi}$ is defined as

$$\mathbf{\Psi}=\begin{bmatrix} 1 \\ v_1 \\ v_2 \\ I+(v_1^2+v_2^2)/2 \end{bmatrix}. \tag{3}$$

The Euler equations are obtained by taking moments of the Boltzmann equation. The 2D Euler equations can be written in the form

$$\frac{\partial \mathbf{U}}{\partial t}+\frac{\partial \mathbf{G}_1}{\partial x_1}+\frac{\partial \mathbf{G}_2}{\partial x_2}=0, \tag{4}$$

where

$$\mathbf{U}=\begin{bmatrix} \rho \\ \rho u_1 \\ \rho u_2 \\ \rho e \end{bmatrix}, \qquad \mathbf{G}_1=\begin{bmatrix} \rho u_1 \\ p+\rho u_1^2 \\ \rho u_1 u_2 \\ u_1(p+\rho e) \end{bmatrix}, \qquad \mathbf{G}_2=\begin{bmatrix} \rho u_2 \\ \rho u_1 u_2 \\ p+\rho u_2 \\ u_2(p+\rho e) \end{bmatrix},$$

$$e=\frac{RT}{\gamma-1}+\tfrac{1}{2}(u_1^2+u_2^2), \qquad p=\text{pressure}=\rho RT.$$

Then

$$\left\langle \mathbf{\Psi}, \frac{\partial F}{\partial t}+v_1\frac{\partial F}{\partial x_1}+v_2\frac{\partial F}{\partial x_2}\right\rangle=\frac{\partial \mathbf{U}}{\partial t}+\frac{\partial \mathbf{G}_1}{\partial x_1}+\frac{\partial \mathbf{G}_2}{\partial x_2}, \tag{5}$$

where the moments are defined as

$$\langle \mathbf{\Psi}, F\rangle \equiv \int_0^\infty \mathrm{d}I \int_{-\infty}^{\infty} \mathrm{d}v_1 \int_{-\infty}^{\infty} \mathrm{d}v_2\, \mathbf{\Psi} F. \tag{6}$$

Therefore we see that

$$\mathbf{U}=\langle \mathbf{\Psi}, F\rangle, \qquad \mathbf{G}_1=\langle \mathbf{\Psi}, v_1 F\rangle, \qquad \mathbf{G}_2=\langle \mathbf{\Psi}, v_2 F\rangle. \tag{7}$$

The KFVS method thus involves two levels, the Boltzmann level and the Euler level, connected by the moments. The implementation of the upwind principle for flux splitting is performed at the Boltzmann level and then mapped to the Euler level. The wall boundary condition too is developed at the Boltzmann level and is based on the specular reflection model of the kinetic theory of gases.[15,17,18] It has been shown that an upwind scheme at the Boltzmann level always gives an upwind scheme at the Euler level.[15]

2.2. *The KFVS finite volume scheme*

A finite volume, cell-centred KFVS scheme has been developed to simulate the flow over bodies of arbitrary shape.[15] For geometrical and adaptive flexibility the scheme has been developed for structured and unstructured grids. In order to develop this scheme, we start with the Euler equations as moments of the Boltzmann equation, which can be written as

$$\left\langle \mathbf{\Psi}, \frac{\partial F}{\partial t}+\mathbf{v}\cdot\frac{\partial F}{\partial \mathbf{x}}\right\rangle=0 \tag{8}$$

where

$$\mathbf{v}=(v_1, v_2)^{\mathrm{T}}, \qquad \mathbf{x}=(x_1, x_2)^{\mathrm{T}}.$$

This can be written in integral form as

$$\iint_A \left\langle \boldsymbol{\Psi}, \frac{\partial F}{\partial t}+\mathbf{v}\cdot\frac{\partial F}{\partial \mathbf{x}} \right\rangle \mathrm{d}x_1\, \mathrm{d}x_2=0$$

or

$$\frac{\partial}{\partial t}\iint_A \langle \boldsymbol{\Psi}, F\rangle\, \mathrm{d}x_1\, \mathrm{d}x_2+\iint_A \left\langle \boldsymbol{\Psi}, \mathbf{v}\cdot\frac{\partial F}{\partial \mathbf{x}} \right\rangle \mathrm{d}x_1\, \mathrm{d}x_2=0. \tag{9}$$

where A is a two-dimensional finite volume with a boundary given by ∂A.

Using the definition of the moments given in equation (6), equation (9) can be written as

$$\frac{\partial}{\partial t}\iint_A \mathrm{d}x_1\, \mathrm{d}x_2 \int_0^\infty \mathrm{d}I \int_{-\infty}^\infty \mathrm{d}v_1 \int_{-\infty}^\infty \mathrm{d}v_2\, \boldsymbol{\Psi}F=-\iint_A \mathrm{d}x_1\, \mathrm{d}x_2 \int_0^\infty \mathrm{d}I \int_{-\infty}^\infty \mathrm{d}v_1 \int_{-\infty}^\infty \mathrm{d}v_2\, \boldsymbol{\Psi}\mathbf{v}\cdot\frac{\partial F}{\partial \mathbf{x}}. \tag{10}$$

Using the divergence theorem, the above equation can be written as

$$\frac{\partial}{\partial t}\iint_A \mathrm{d}x_1\, \mathrm{d}x_2 \int_0^\infty \mathrm{d}I \int_{-\infty}^\infty \mathrm{d}v_1 \int_{-\infty}^\infty \mathrm{d}v_2\, \boldsymbol{\Psi}F=-\iint_{\partial A} \mathrm{d}s \int_0^\infty \mathrm{d}I \int_{-\infty}^\infty \mathrm{d}v_1 \int_{-\infty}^\infty \mathrm{d}v_2\, \boldsymbol{\Psi}\mathbf{v}\cdot\mathbf{n}F, \tag{11}$$

where ds is an element on the boundary and $\mathbf{n}$ is the unit outward normal.

Let us now consider a single finite volume bounded by K sides. Each side s_k, $k=1, \ldots, K$, has the outward normal $\mathbf{n}_k$. Using equation (7) for the left-hand side, equation (11) can now be written as

$$|A|\frac{\partial \mathbf{U}}{\partial t}=-\sum_{k=1}^{K}\int_0^\infty \mathrm{d}I \int_{-\infty}^\infty \mathrm{d}v_1 \int_{-\infty}^\infty \mathrm{d}v_2\, \boldsymbol{\Psi}\mathbf{v}\cdot\mathbf{n}_k\, |s_k|\, F, \tag{12}$$

where $|A|$ is the area of the finite volume and $|s_k|$ is the length of side s_k. $\mathbf{U}$ represents the field vector at the centroid of the finite volume. Let θ_k be the angle between side s_k and the positive x-axis. The normal and tangential velocity components $v_{\mathrm{n}k}$ and $v_{\mathrm{t}k}$ are then related to v_1 and v_2 by

$$v_1=v_{\mathrm{t}k}\cos\theta_k+v_{\mathrm{n}k}\sin\theta_k, \qquad v_2=v_{\mathrm{t}k}\sin\theta_k-v_{\mathrm{n}k}\cos\theta_k. \tag{13}$$

Using equation (13), the moment vector $\boldsymbol{\Psi}$ defined in equation (3) can be rewritten as

$$\boldsymbol{\Psi}_k=\begin{bmatrix} 1 \\ v_{\mathrm{t}k}\cos\theta_k+v_{\mathrm{n}k}\sin\theta_k \\ v_{\mathrm{t}k}\sin\theta_k-v_{\mathrm{n}k}\cos\theta_k \\ I+(v_{\mathrm{t}k}^2+v_{\mathrm{n}k}^2)/2 \end{bmatrix}, \tag{14}$$

where $\boldsymbol{\Psi}_k$ is now the moment vector for side s_k. Since the Maxwellian velocity distribution is invariant under co-ordinate rotation, equation (12) can be written as

$$\frac{\partial \mathbf{U}}{\partial t}|A|=-\sum_{k=1}^{K}\int_0^\infty \mathrm{d}I \int_{-\infty}^\infty \mathrm{d}v_{\mathrm{t}k} \int_{-\infty}^\infty \mathrm{d}v_{\mathrm{n}k}\, \boldsymbol{\Psi}_k\, v_{\mathrm{n}k}\, |s_k|\, F_{sk}, \tag{15}$$

where F_{sk} is the Maxwellian written in terms of v_{nk} and v_{tk}, for side s_k. The above equation can be further rewritten as

$$\frac{\partial \mathbf{U}}{\partial t}|A| = -\sum_{k=1}^{K} |s_k|\, \mathbf{G}_{sk}, \tag{16}$$

where

$$\mathbf{G}_{sk} = \langle \boldsymbol{\Psi}_k, v_{nk} F_{sk} \rangle . \tag{17}$$

As mentioned earlier, the splitting of the fluxes based on the upwind principle is done at the Boltzmann level and then mapped to the Euler level. In order to explain this clearly, let us consider a triangular volume with sides s_1, s_2 and s_3. It may be noted that the analysis given below is valid for a finite volume with any number of sides. Figure 1 shows this triangular volume 1 surrounded by three other similar volumes 2, 3 and 4.

The fluxes are split on the basis of whether the normal velocity v_{nk} is positive or negative. It should be noted that v_{nk} and v_{tk} represent the molecular and not the fluid velocity. For side s_1 we can write

$$v_{n1}\, F_{s1} = \frac{v_{n1} + |v_{n1}|}{2} F_{s1}^{\text{out}} + \frac{v_{n1} - |v_{n1}|}{2} F_{s1}^{\text{in}}, \tag{18}$$

where F_{s1}^{out} denotes the part of the Maxwellian corresponding to $v_{n1} > 0$ and F_{s1}^{in} denotes the part of the Maxwellian corresponding to $v_{n1} < 0$. Taking moments of equation (18),

$$\langle \boldsymbol{\Psi}, v_{n1} F_{s1} \rangle = \left\langle \boldsymbol{\Psi}, \frac{v_{n1} + |v_{n1}|}{2} F_{s1}^{\text{out}} \right\rangle + \left\langle \boldsymbol{\Psi}, \frac{v_{n1} - |v_{n1}|}{2} F_{s1}^{\text{in}} \right\rangle = \mathbf{G}_{s1}^{+} + \mathbf{G}_{s1}^{-}, \tag{19}$$

where $\mathbf{G}_{s1}^{+}$ and $\mathbf{G}_{s1}^{-}$ are the split Euler fluxes across side s_1. The upwind principle now determines where these fluxes are evaluated. Referring to Figure 1, for side s_1 it is necessary to evaluate $\mathbf{G}_{s1}^{+}$ at the centroid of triangle 1 and $\mathbf{G}_{s1}^{-}$ at the centroid of triangle 2. Similar arguments for sides s_2 and s_3 give

$$\mathbf{G}_{s1} = [\mathbf{G}_{s1}^{+}]_1 + [\mathbf{G}_{s1}^{-}]_2, \qquad \mathbf{G}_{s2} = [\mathbf{G}_{s2}^{+}]_1 + [\mathbf{G}_{s2}^{-}]_3, \qquad \mathbf{G}_{s3} = [\mathbf{G}_{s3}^{+}]_1 + [\mathbf{G}_{s3}^{-}]_4, \tag{20}$$

where $[\mathbf{G}_{sk}^{+}]_m$ is the positive flux across side s_k evaluated at the centroid of triangle m. The first-order KFVS finite volume scheme can be written using equation (16) as

$$\mathbf{U}^{n+1} = \mathbf{U}^{n} - \frac{\Delta t}{|A|} \sum_{k=1}^{3} |s_k|\, \mathbf{G}_{sk}, \tag{21}$$

where $\mathbf{G}_{sk}$ is given in equation (20), $\mathbf{U}^n$ is the field vector at time level n and Δt is the time step.

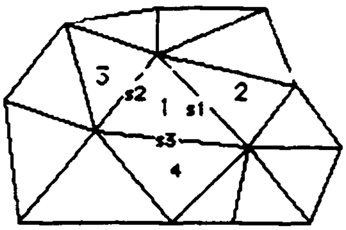

Figure 1. Typical triangulation with cell 1 and the surrounding cells 2, 3 and 4

Referring to equations (15)–(19), the split fluxes across side s_k are given by

$$\mathbf{G}_{sk}^{+}=\int_0^{\infty}\mathrm{d}I\int_{-\infty}^{\infty}\mathrm{d}v_{tk}\int_0^{\infty}\mathrm{d}v_{nk}\,\Psi_k\,v_{nk}\,F_{sk},\qquad \mathbf{G}_{sk}^{-}=\int_0^{\infty}\mathrm{d}I\int_{-\infty}^{\infty}\mathrm{d}v_{tk}\int_{-\infty}^{0}\mathrm{d}v_{nk}\,\Psi_k\,v_{nk}\,F_{sk}. \tag{22}$$

The detailed calculations showing how the split fluxes are obtained are not given here. The final expressions for the various fluxes in terms of the flow variables are given below:

$$\mathbf{G}_{sk}^{\pm}=\begin{bmatrix} \rho u_{nk}A_k^{\pm}\pm\rho B_k \\ \sin\theta_k[(p+\rho u_{nk}^2)A_k^{\pm}\pm\rho u_{nk}B_k]+\rho\cos\theta_k(u_{nk}u_{tk}A_k^{\pm}\pm u_{tk}B_k) \\ -\cos\theta_k[(p+\rho u_{nk}^2)A_k^{\pm}\pm\rho u_{nk}B_k]+\rho\sin\theta_k(u_{nk}u_{tk}A_k^{\pm}\pm u_{tk}B_k) \\ \{[\gamma/(\gamma-1)]p+\tfrac{1}{2}\rho(u_{nk}^2+u_{tk}^2)\}u_{nk}A_k^{\pm}\pm\{[(\gamma+1)/2(\gamma-1)]p+\tfrac{1}{2}\rho(u_{nk}^2+u_{tk}^2)\}B_k \end{bmatrix}, \tag{23}$$

where

$$A_k^{\pm}=\frac{1\pm\operatorname{erf}s_{nk}}{2},\qquad B_k=\frac{e^{-s_{nk}^2}}{2\sqrt{(\pi)\beta}},\qquad s_{nk}=u_{nk}\sqrt{\beta}.$$

The KFVS scheme described above is a finite volume, cell-centred scheme and requires an appropriate data structure for implementation on unstructured meshes. An edge/cell data structure is used in which the two mesh points forming each edge, as well as the two cells adjacent to the edge, are stored in the mesh connectivity matrix. The appropriate flux calculated at each edge is sent to the neighbouring cells and the algorithm then requires a loop over all the edges contained in the mesh. Boundary edges are identified so that the correct flux is determined. The flux at a solid wall is determined by the use of a flow tangency boundary condition which is described later. The flux at the far-field boundary is determined by the theory of Riemann invariants.

2.3. *The KFVS high-resolution scheme*

A high-resolution KFVS scheme has been developed[15,16] and is described below. Implementation of this scheme is straightforward for a structured, quadrilateral mesh but requires additional thought and effort for an unstructured, triangular mesh. The scheme is first discussed for a structured mesh and the extension to an unstructured mesh is discussed later.

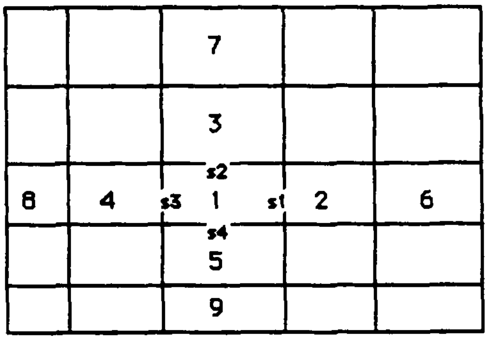

Figure 2. Schematic of a structured mesh showing the cells used in the high-resolution scheme

A typical structured mesh is shown in Figure 2. From this figure the first-order KFVS scheme discussed above will give, for mesh cell 1

$$\mathbf{U}^{n+1}=\mathbf{U}^{n}-\frac{\Delta t}{|A|}\sum_{k=1}^{4}|s_k|\,\mathbf{G}_{sk}, \tag{24}$$

where

$$\mathbf{G}_{s1}=[\mathbf{G}^{+}_{s1}]_1+[\mathbf{G}^{-}_{s1}]_2,\qquad \mathbf{G}_{s2}=[\mathbf{G}^{+}_{s2}]_1+[\mathbf{G}^{-}_{s2}]_3,\qquad \mathbf{G}_{s3}=[\mathbf{G}^{+}_{s3}]_1+[\mathbf{G}^{-}_{s3}]_4,$$
$$\mathbf{G}_{s4}=[\mathbf{G}^{+}_{s4}]_1+[\mathbf{G}^{-}_{s4}]_5. \tag{25}$$

The high-resolution scheme requires cells 6, 7, 8 and 9, which are known for a structured mesh. The flux at any edge s_k is now evaluated by extrapolation from the two adjacent cells. Let D_{ab} represent the distance between the centroids of any two cells 'a' and 'b' and D_{ask} represent the distance between the centroid of any cell 'a' and the midpoint of edge s_k. The flux $\mathbf{G}_{s1}$ is now given by

$$\mathbf{G}_{s1}=[\mathbf{G}^{+}_{s1}]_1+\frac{D_{1s1}}{D_{14}}([\mathbf{G}^{+}_{s1}]_1-[\mathbf{G}^{+}_{s1}]_4)+[\mathbf{G}^{-}_{s1}]_2+\frac{D_{2s1}}{D_{26}}([\mathbf{G}^{-}_{s1}]_2-[\mathbf{G}^{-}_{s1}]_6). \tag{26}$$

Fluxes $\mathbf{G}_{s2}$, $\mathbf{G}_{s3}$ and $\mathbf{G}_{s4}$ are obtained similarly. This scheme can cause oscillations around the shock wave[15] and is modified by the use of a minmod limiter which is defined by

$$\operatorname{minmod}(a,b)=\begin{cases}a & \text{if } |a|\leqslant|b|,\\ b & \text{if } |b|<|a|.\end{cases} \tag{27}$$

The flux $\mathbf{G}_{s1}$ is now given by

$$\begin{aligned}\mathbf{G}_{s1}=[\mathbf{G}^{+}_{s1}]_1&+\operatorname{minmod}\left(\frac{D_{1s1}}{D_{14}}([\mathbf{G}^{+}_{s1}]_1-[\mathbf{G}^{+}_{s1}]_4),\ \Phi\frac{D_{1s1}}{D_{12}}([\mathbf{G}^{+}_{s1}]_2-[\mathbf{G}^{+}_{s1}]_1)\right)\\ &+[\mathbf{G}^{-}_{s1}]_2+\operatorname{minmod}\left(\frac{D_{2s1}}{D_{26}}([\mathbf{G}^{-}_{s1}]_2-[\mathbf{G}^{-}_{s1}]_6),\ \Phi\frac{D_{2s1}}{D_{12}}([\mathbf{G}^{-}_{s1}]_1-[\mathbf{G}^{-}_{s1}]_2)\right),\end{aligned} \tag{28}$$

where Φ is a factor with a typical value of 1·4. $\mathbf{G}_{s2}$, $\mathbf{G}_{s3}$ and $\mathbf{G}_{s4}$ are obtained similarly.

Figure 1 shows a typical unstructured mesh. Cells 2, 3 and 4 are known from the edge/cell data structure, but the additional cells needed for implementing the high-resolution scheme for cell 1 are unknown. The implementation of the high-resolution scheme, as described above for a structured mesh, requires that for each edge the two adjacent cells on both sides be known. Referring to Figure 2, for edge s_1, cells 4 and 1 on one side and cells 2 and 6 on the other side are needed. The analogous situation in an unstructured mesh, as shown in Figure 3, requires that for edge s_1, cells 1 and 4 on one side and cells 2 and 3 on the other side need to be known for an appropriate extrapolation of the flow variables.

The edge/cell-based data structure gives cells 1 and 2 for edge s_1. A procedure has been evolved for the determination of the other two cells for each edge. The cells adjoining the edge, namely cells 1 and 2, are identified from the data structure. Then the third vertex of each cell is found, i.e. the vertex not contained in the common edge. All cells containing this third vertex are then located by a search through all the edges. This locates the cells marked '*' on one side of s_1 and the cells marked '+' on the other side. To now find cell 3, the following method is used. The slope of the straight line joining the centre of edge s_1 to the centroid of cell 2 is evaluated. The slopes of the straight lines joining the centroid of cell 2 to the centroids of all the cells marked '*' are then evaluated. The cell with the slope closest to the slope between edge s_1 and cell 2, is taken to

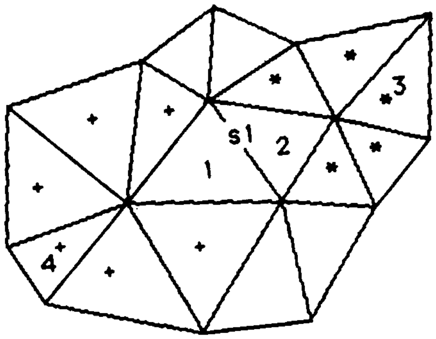

Figure 3. Unstructured mesh showing the cells used for the high-resolution scheme

be cell 3. Cell 4 is determined in a similar manner and these two 'high-resolution cells' are identified for each interior edge. The high-resolution scheme is then implemented in the same way as on a structured mesh.

2.4. *Boundary condition at wall*

A flow tangency boundary condition called the kinetic characteristic boundary condition (KCBC) has been developed.[15,17] This is based on the specular reflection model of the kinetic theory of gases, according to which the normal component of the velocity of a molecule gets reversed after impact with the wall while the tangential component of the velocity remains unchanged. The flux for the edge which lies on a solid wall is calculated in a manner similar to the calculations for the split fluxes described earlier.

Let θ_w be the angle between the edge s_w and the positive x-axis. Referring to equations (14) and (17), the flux across s_w is

$$\mathbf{G}_w = \langle \mathbf{\Psi}_w, v_{nw} F_{sw} \rangle, \tag{29}$$

where

$$\mathbf{\Psi}_w = \begin{bmatrix} 1 \\ v_{tw}\cos\theta_w + v_{nw}\sin\theta_w \\ v_{tw}\sin\theta_w - v_{nw}\cos\theta_w \\ I + (v_{tw}^2 + v_{nw}^2)/2 \end{bmatrix} \tag{30}$$

and v_{tw} and v_{nw} represent the tangential and normal components of the molecular velocity.

Let the velocity distribution function F_{sw} be denoted by $F_{\rm I}$ for molecules which are incident to the wall and by $F_{\rm R}$ for molecules which are reflected from the wall. According to the reflection model, the two are related by

$$F_{\rm R}(v_{tw}, v_{nw}, I) = F_{\rm I}(v_{tw}, -v_{nw}, I). \tag{31}$$

Referring to equations (15) and (17), equation (29) is written as

$$\mathbf{G}_w = \int_0^\infty dI \int_{-\infty}^{\infty} dv_{tw} \int_{-\infty}^{\infty} dv_{nw}\, \mathbf{\Psi}_w v_{nw} F_{sw}. \tag{32}$$

The velocity distribution function is split into two parts which correspond to molecules incident to and reflected from the wall. The above equation is written as

$$\mathbf{G}_{\mathrm{w}}=\int_0^{\infty}\mathrm{d}I\int_{-\infty}^{\infty}\mathrm{d}v_{\mathrm{tw}}\left(\int_0^{\infty}\mathrm{d}v_{\mathrm{nw}}\,\boldsymbol{\Psi}_{\mathrm{w}}\,v_{\mathrm{nw}}\,F_{\mathrm{I}}+\int_{-\infty}^{0}\mathrm{d}v_{\mathrm{nw}}\,\boldsymbol{\Psi}_{\mathrm{w}}\,v_{\mathrm{nw}}\,F_{\mathrm{R}}\right),\tag{33}$$

which, using equation (31), is rewritten as

$$\mathbf{G}_{\mathrm{w}}=\int_0^{\infty}\mathrm{d}I\int_{-\infty}^{\infty}\mathrm{d}v_{\mathrm{tw}}\left(\int_0^{\infty}\mathrm{d}v_{\mathrm{nw}}\,\boldsymbol{\Psi}_{\mathrm{w}}\,v_{\mathrm{nw}}\,F_{\mathrm{sw}}(v_{\mathrm{tw}},v_{\mathrm{nw}},I)+\int_{-\infty}^{0}\mathrm{d}v_{\mathrm{nw}}\,\boldsymbol{\Psi}_{\mathrm{w}}\,v_{\mathrm{nw}}\,F_{\mathrm{sw}}(v_{\mathrm{tw}},-v_{\mathrm{nw}},I)\right).\tag{34}$$

Evaluation of this equation gives the flux across the wall in terms of the flow variables as

$$\mathbf{G}_{\mathrm{w}}=\begin{bmatrix}0\\ 2\sin\theta_{\mathrm{w}}[(p+\rho u_{\mathrm{nw}}^2)A_{\mathrm{w}}^{+}+\rho u_{\mathrm{nw}}B_{\mathrm{w}}]\\ -2\cos\theta_{\mathrm{w}}[(p+\rho u_{\mathrm{nw}}^2)A_{\mathrm{w}}^{+}+\rho u_{\mathrm{nw}}B_{\mathrm{w}}]\\ 0\end{bmatrix},\tag{35}$$

where

$$A=\frac{1+\operatorname{erf}s_{\mathrm{nw}}}{2},\qquad B=\frac{\mathrm{e}^{-s_{\mathrm{nw}}^2}}{2\sqrt{(\pi)\beta}},\qquad s_{\mathrm{nw}}=u_{\mathrm{nw}}\sqrt{\beta}.$$

Implementation of this boundary condition, which is first-order accurate, does not require the use of any dummy cells.

2.5. *Effect of the high-resolution scheme*

The high-resolution scheme seems to be essential for capturing shock waves in transonic supercritical flows. This is illustrated for a flow around a NACA 0012 aerofoil with a freestream Mach number of 0·75 and an incidence angle of 2°. The grid used is shown in Figure 4. Figure 5 shows the C_{p}-values on the surface of the aerofoil obtained by the first-order scheme and Figure 6 shows the same values obtained by the high-resolution scheme. The figures show that the first-order scheme is unable to resolve the flow features for these cases. This is not so for supersonic flows, where it has been observed that there is an insignificant difference between the first-order and high-resolution schemes.

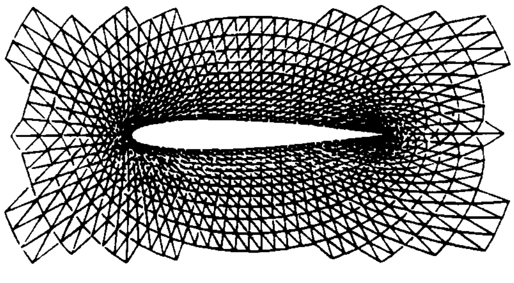

Figure 4. Regular triangulation

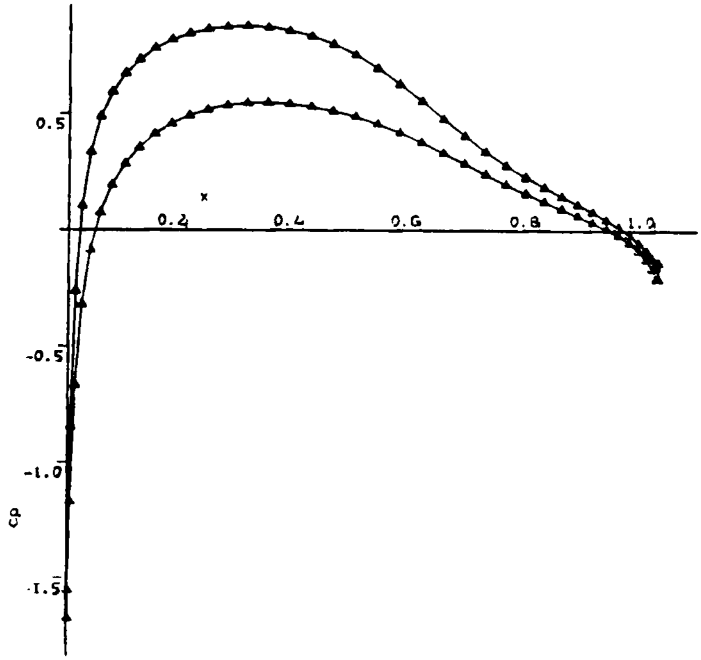

Figure 5. NACA 0012, $M=0{\cdot}75$, $\alpha=2{\cdot}0°$: C_p using KFVS first-order scheme

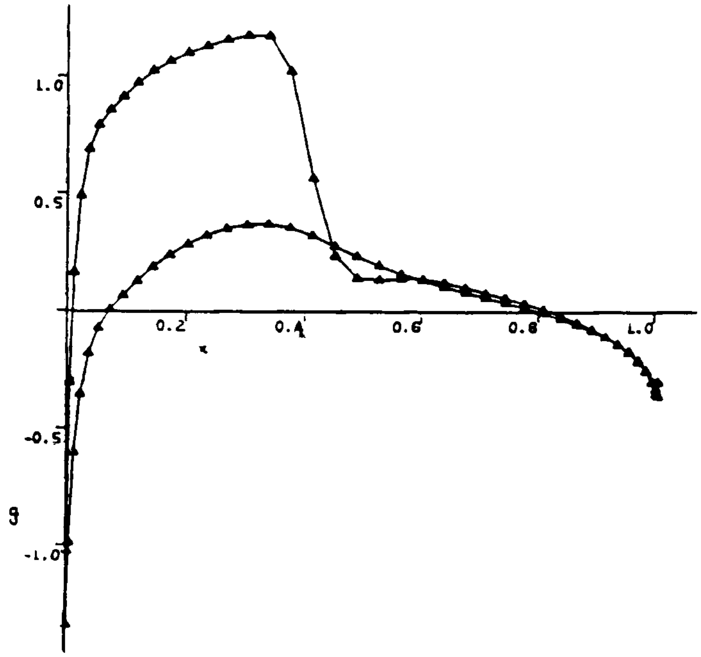

Figure 6. NACA 0012, $M=0{\cdot}75$, $\alpha=2{\cdot}0°$: C_p using KFVS high-resolution scheme

The effect of using the minmod limiter in the high-resolution scheme is less dramatic. The use of the limiter significantly increases the computational effort required and it is essential to investigate its advantages. The test case is again the flow over a NACA 0012 aerofoil with a freestream Mach number of 0·8 and an incidence angle of 1·25° where the mesh used is as before (Figure 4). Figures 7 and 8 show the C_p-plot and convergence history respectively when the limiter is not used and Figures 9 and 10 show the same when the limiter is used. The residual used here is the norm of the relative change in the pressure, and the logarithm of this value is plotted. A comparison of Figures 7 and 9 shows that the minmod limiter does suppress the preshock spike. Figures 8 and 10 show that the use of the limiter dramatically changes the convergence behaviour of the KFVS scheme. A large number of iterations have been performed for these computations to ensure adequately converged results.

2.6. Solution process

The KFVS finite volume scheme described earlier uses explicit Euler time stepping to reach steady state. Each mesh cell is advanced by a local time step which is limited by the requirements for a stable scheme. The stability of the KFVS method has been determined for a structured mesh.[15]

The stability condition for the first-order KFVS finite volume scheme can be written as

$$\Delta t \leqslant |A_{ij}| \Bigg/ \left(\sum_{k=1}^{4} [u_{nk} + 3\sqrt{(RT)}]\,|s_k| \right). \tag{36}$$

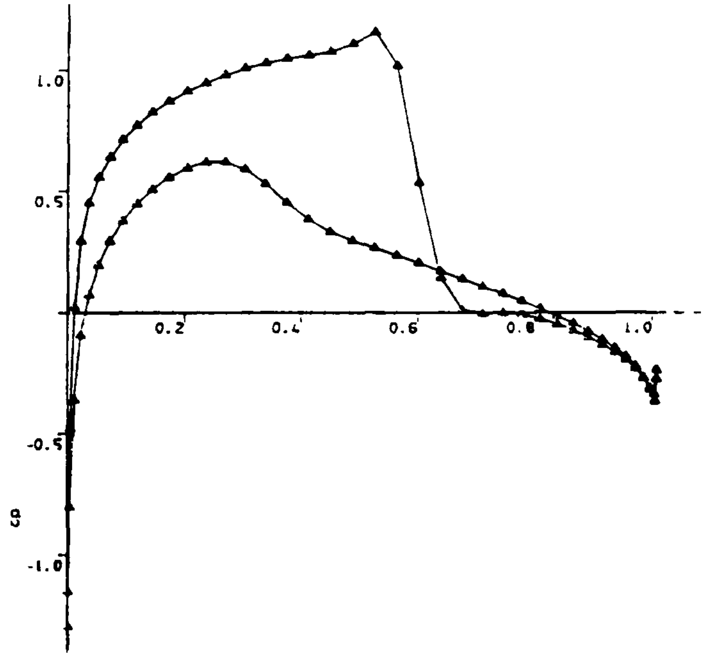

Figure 7. NACA 0012, $M=0{\cdot}80$, $\alpha=1{\cdot}25°$: C_p using KFVS without minmod limiter

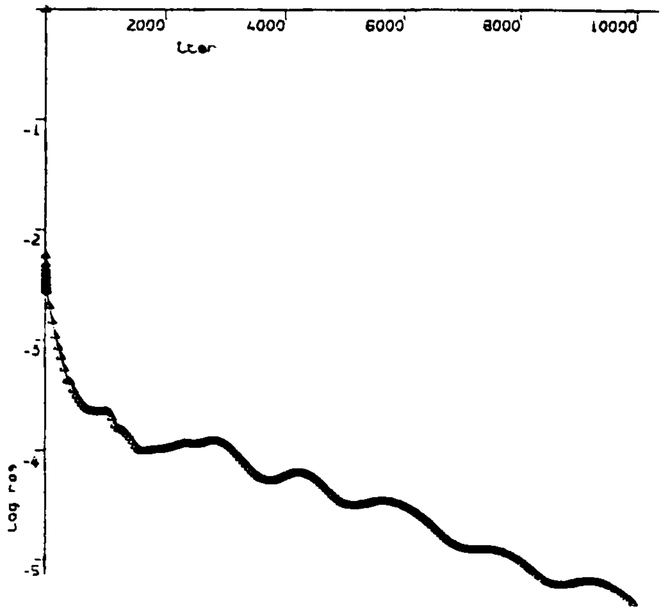

Figure 8. NACA 0012, $M=0{\cdot}80$, $\alpha=1{\cdot}25°$: convergence without minmod limiter

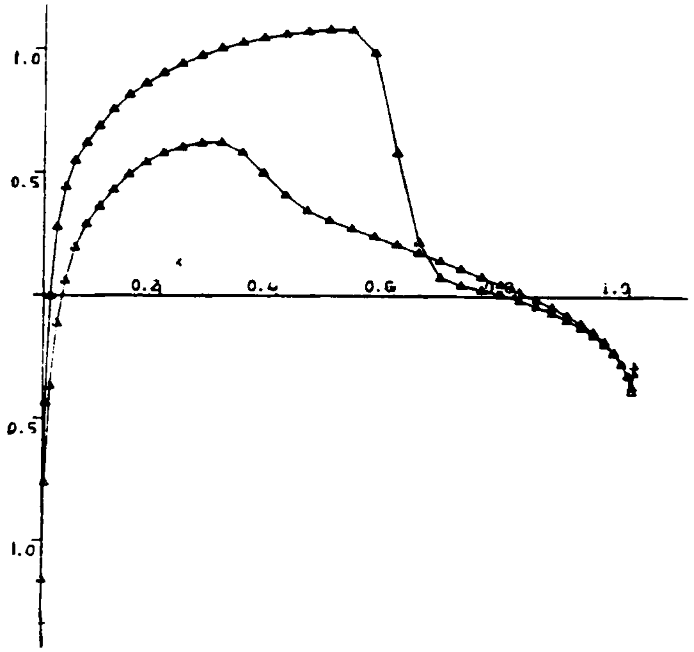

Figure 9. NACA 0012, $M=0{\cdot}80$, $\alpha=1{\cdot}25°$: C_p using KFVS with minmod limiter

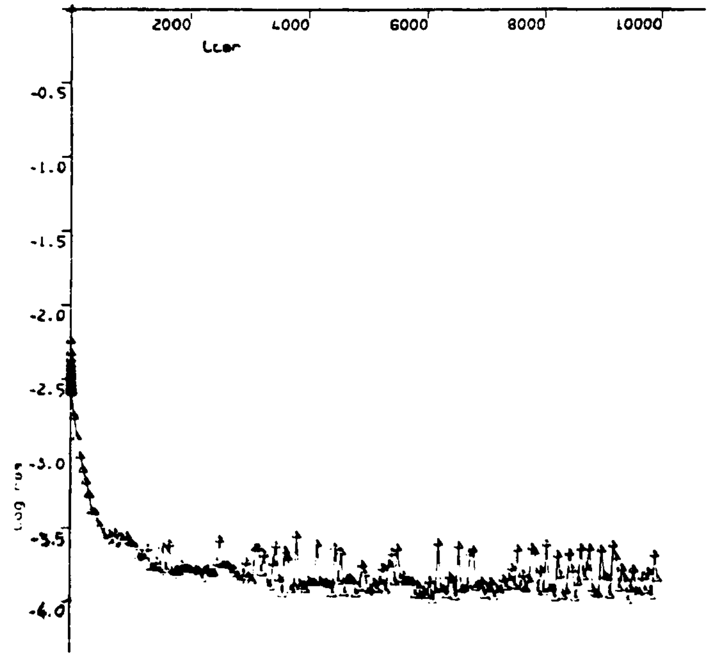

Figure 10. NACA 0012, $M=0{\cdot}80$, $\alpha=1{\cdot}25°$: convergence with minmod limiter

A similar analysis for the high-resolution scheme would be quite cumbersome and the multiplication of the time step evaluated above by a factor less than unity has been proposed.[15] A factor of 0·7 has generally been used.

For unstructured meshes any similar stability analysis is difficult. A rigorous mathematical analysis has not been attempted. Instead, essentially the same stability condition has been used as given in equation (36), with, of course, the summation on the right-hand side being over three rather than four bounding edges for a mesh consisting of triangles. This condition has been used for all the results presented in this paper. It is possible that this imposes a stricter limit on the time step than is actually needed, but no attempt has been made to investigate this.

3. MESH GENERATION

3.1. Delaunay triangulation

The automatic triangulation of an arbitrary set of points can be achieved using the Delaunay triangulation. Since this method was first proposed for application in CFD,[22] robust algorithms to construct the triangulation in both two and three dimensions have been developed.[23,24,25] In common with other unstructured grid techniques the Delaunay approach offers the advantages of flexibility for highly complex shapes and mesh adaptation.

The triangulation is based upon the concepts of the in-circle criterion. The triangulation is the geometrical dual of the Voronoi diagram. This diagram is the construction of tiles in which a region is associated with every point in such a way that each region is closer to a point than to any other point in the field. The bounding line segments form the Voronoi diagram. If points with common line segments are connected, then the Delaunay triangulation is formed. The vertices of the Voronoi diagram are at the centres of the circles passing through three points which form the individual triangles. No other points can lie within a circle. The triangulation possesses some interesting mathematical properties and ensures the optimally smooth triangulation of an arbitrary set of points.

The approach outlined above can be used in generating two contrasting grid types. Firstly, if points from a structured mesh generator are used in the Delaunay algorithm, a regular triangulation is obtained. Historically, this was the method first used to provide a mesh around a complex shape.[25] Around each individual component of a configuration a structured set of grid points was generated. The global mesh was obtained by connecting together points from all component meshes. This approach is utilized in this work since it proves to generate very regular and smooth meshes. The above approach is not readily applicable to any arbitrary shape and hence a new flexible procedure for automatic point generation has been developed.[24] This approach constructs a distribution of points in the interior of the domain which is consistent with the boundary point distribution. This approach is also utilized in this work.

3.2. *Mesh adaptation*

Mesh adaptation is an important procedure in numerical flow simulation. It offers the prospect of accurate flow field simulations without the use of excessively fine, computationally expensive meshes. The implementation of adaptive meshing requires two basic steps. Firstly, the identification of an error or adaptivity criterion which indicates where in the flow field the mesh is deficient and requires some modification. Changes in the mesh may be required where the activity is high or where the activity is sufficiently low that fewer grid points are required. Secondly, it is necessary to use the mechanics of mesh generation to suitably modify the mesh. Most adaptation procedures are based upon the equidistribution principle. Throughout the field the product of the adaptivity criterion and the local mesh length scale should be constant. Hence in regions of high activity the local mesh length scale should be small, whilst in regions of low activity the length scale should be large.

Of the many methods available for mesh adaptation[26] the mesh enrichment technique is fairly easy to implement on unstructured meshes and has been coupled with the KFVS solver. This technique involves the addition of extra mesh points in regions of high flow gradients.

The gradient across an edge is computed as

$$\Delta \equiv \frac{\rho(\mathrm{N2})-\rho(\mathrm{N1})}{\rho(\mathrm{N2})+\rho(\mathrm{N1})}, \tag{37}$$

where the flow variable ρ, the density, has been chosen as the refinement indicator. The edge is then divided if $|\Delta| \geqslant A_{\mathrm{R}}$, where A_{R} is a specified parameter with a value normally between 0·05 and 0·2. If refinement occurs, the edge is divided by the insertion of a new point at the midpoint of edge E and the formation of two new cells. This formulation requires the interpolation of the density from the cell centres to the cell vertices. This proves to provide a better, more consistent refinement of the mesh.

4. RESULTS

4.1. *Williams two-component aerofoil—low subsonic flow*

The first test case considered is the flow over a two-component aerofoil with a freestream Mach number of 0·15 and zero incidence angle. The mesh used is a regular pseudo-unstructured mesh generated by the triangulation of a set of points around the aerofoil. The flexibility of unstructured meshes makes the mesh generation relatively simple.

The mesh contains 2143 mesh points and is shown in Figure 11. The Mach contours obtained by the KFVS method are shown in Figure 12 and the coefficient of pressure on the surface of the aerofoil and flap is shown in Figures 13 and 14 respectively. It is seen that the method produces smooth contours of flow and surface pressure distributions.

4.2. NACA 0012 aerofoil—transonic flow

The case considered now is the supercritical flow over a NACA 0012 aerofoil with a freestream Mach number of 0·85 and an incidence angle of 1·25°. The results are compared with those obtained by a Jameson centred scheme.[5,7] The mesh shown in Figure 15 is used for the first set of results shown. This is an unstructured mesh containing 2372 mesh points. The flow contours of pressure obtained by the KFVS and Jameson schemes are shown in Figures 16 and 17 respectively. A comparison of the two shows that the KFVS method generally gives smoother flow contours while the Jameson scheme has better captured the shock waves on both surfaces of the aerofoil. The coefficient of pressure on the aerofoil surface obtained by the KFVS scheme is compared with the Jameson result in Figure 18. The KFVS result shows some oscillations in the pressure distribution which are not present in the Jameson result and also shows a slightly different shock wave position on the upper surface.

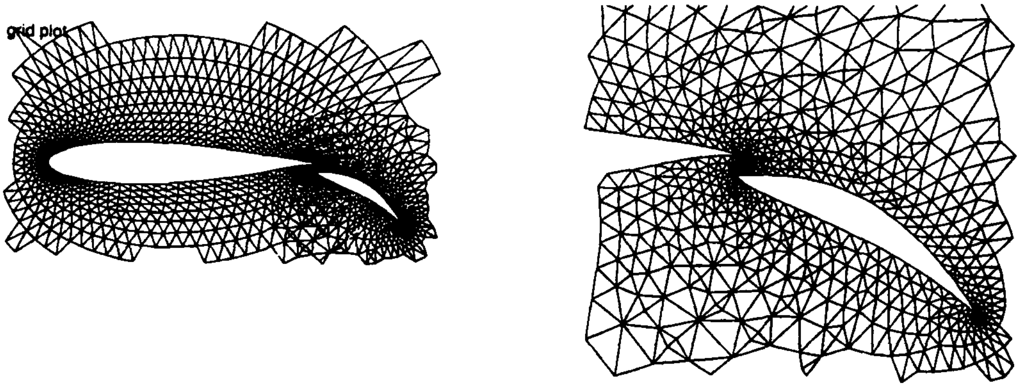

Figure 11. Regular mesh, Williams aerofoil

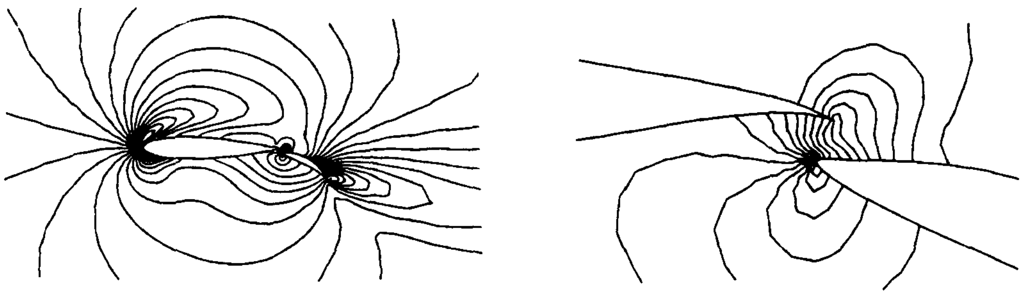

Figure 12. Mach number contours on regular mesh

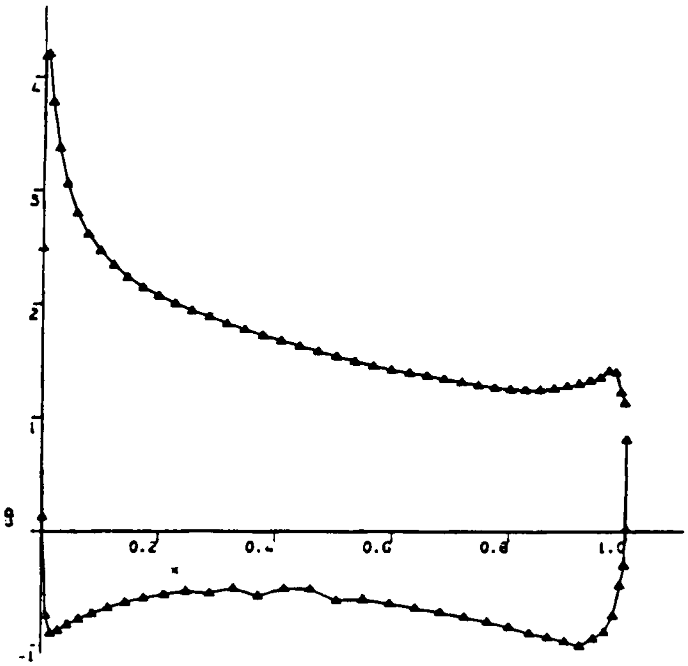

Figure 13. Pressure coefficient C_p, first component

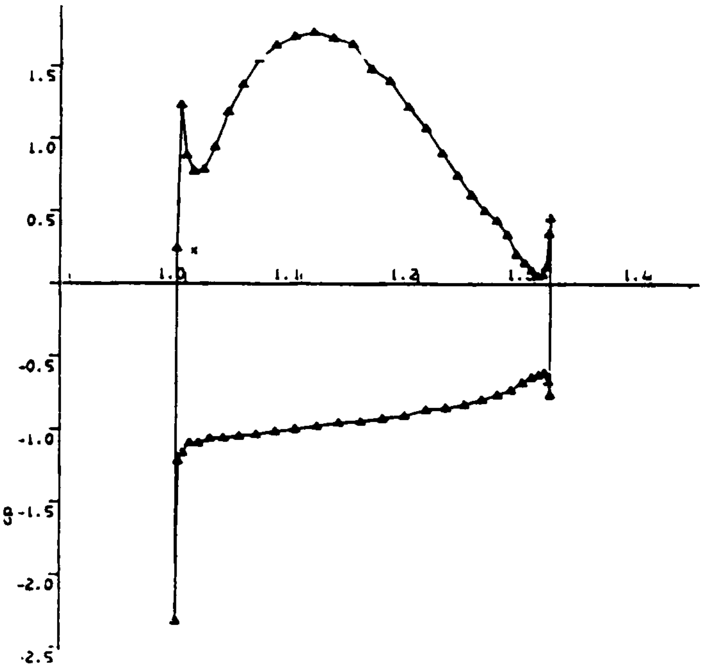

Figure 14. Pressure coefficient C_p, second component

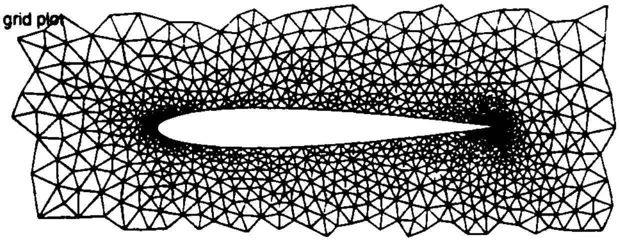

Figure 15. Unstructured mesh, NACA 0012 aerofoil

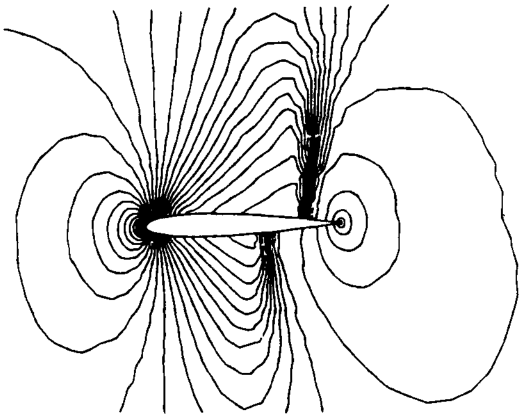

Figure 16. Contours of pressure (KFVS)

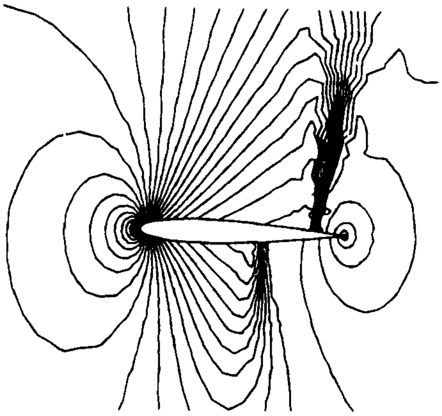

Figure 17. Contours of pressure (Jameson)

This particular test case, with shock waves present on both surfaces of the aerofoil, is ideal for the application of mesh adaptivity. The local mesh enrichment technique used is one where mesh points are added to regions of high flow gradients. It is reasonable to start with a very coarse mesh, which is unable to adequately resolve the features of the flow, and adapt it to a mesh capable of the resolution required. The initial mesh, shown in Figure 19, contains 1182 mesh points. The contours of pressure obtained on this mesh are shown in Figure 20. The mesh obtained after two levels of refinement is shown in Figure 21. This mesh now contains 2309 mesh points. The contours of pressure obtained on this mesh (Figure 22) show a remarkable improve-

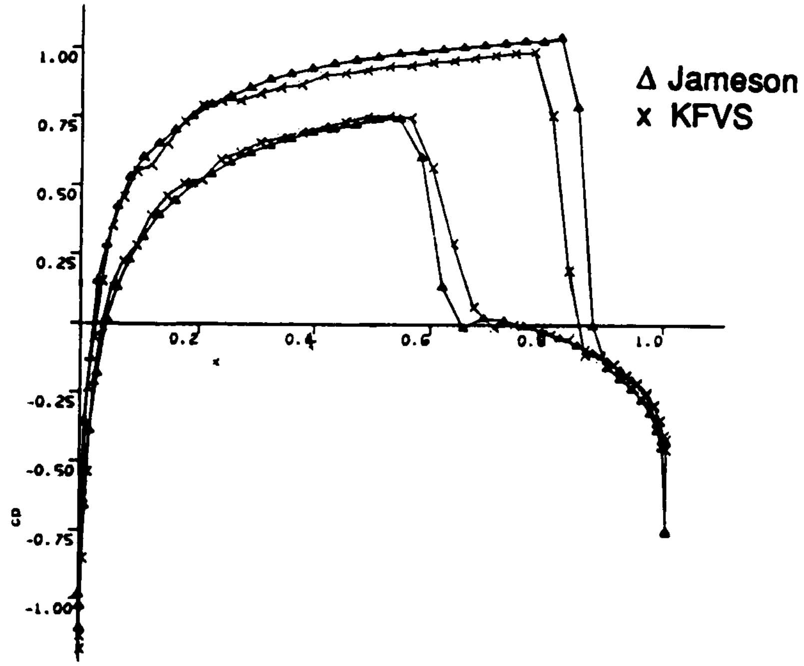

Figure 18. Comparison of pressure coefficient

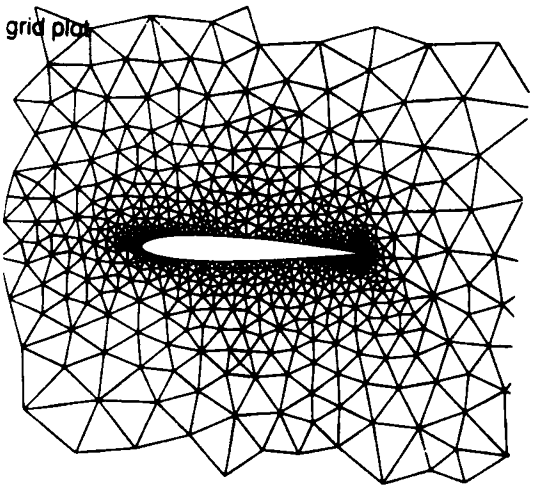

Figure 19. Initial mesh

ment over the earlier results, with much sharper shock waves captured on both the upper and lower surfaces of the aerofoil.

4.3. Internal flow in a channel—supersonic flow

In order to test the KFVS flow algorithm for a variety of flow situations, the flow in a channel containing a 10·75° ramp with a freestream Mach number of 2·0 has been solved. This particular case also highlights the effectiveness of mesh adaptivity when used with the KFVS method.

Figure 23 shows the initial mesh and the flow contours of density obtained. This mesh contains 446 mesh points with 93 points on the boundary. The solution obtained on this mesh is quite poor. Figures 24–26 show the mesh and the corresponding contours of density, after one, two and

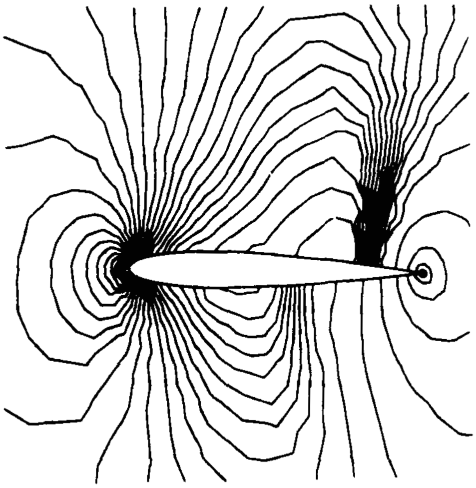

Figure 20. Contours of pressure on initial mesh

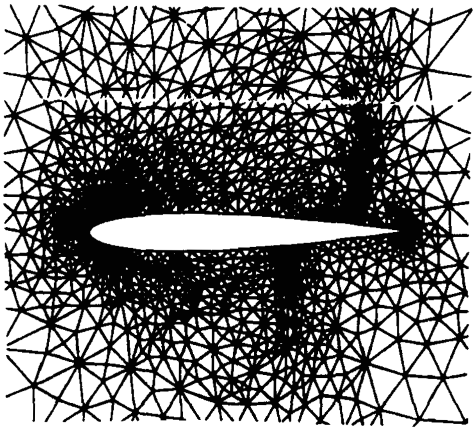

Figure 21. Refined mesh

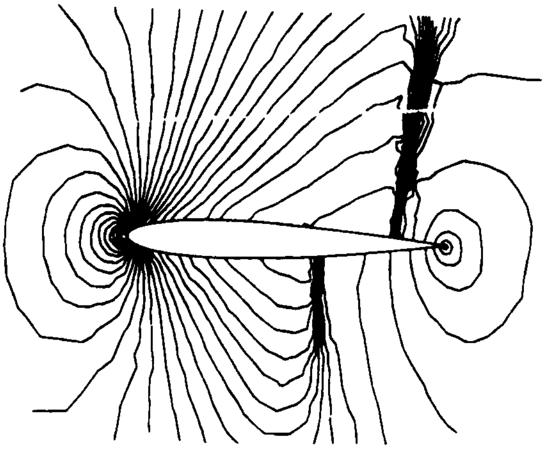

Figure 22. Contours of pressure on refined mesh

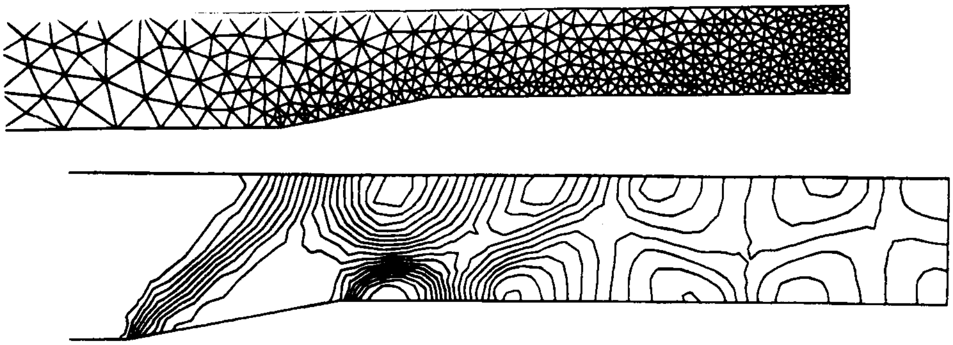

Figure 23. Initial mesh and contours of density

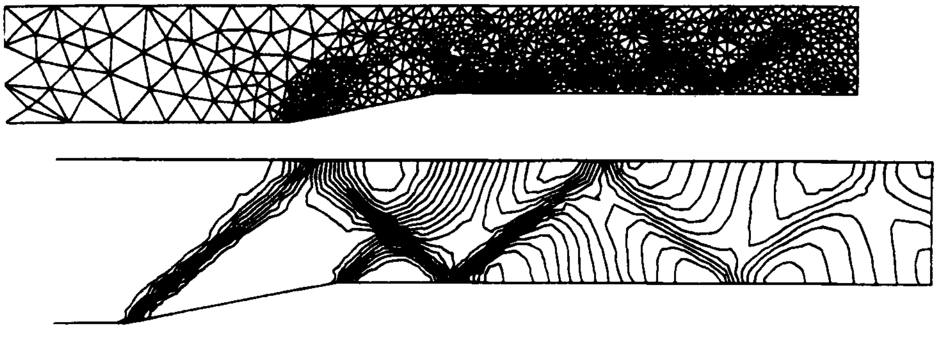

Figure 24. First refined mesh and contours of density

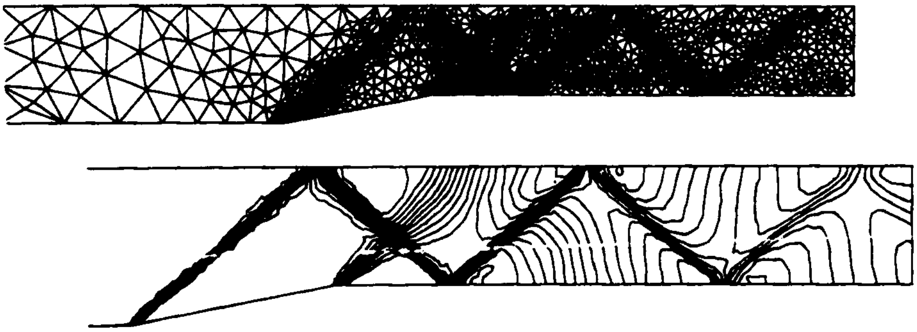

Figure 25. Second refined mesh and contours of density

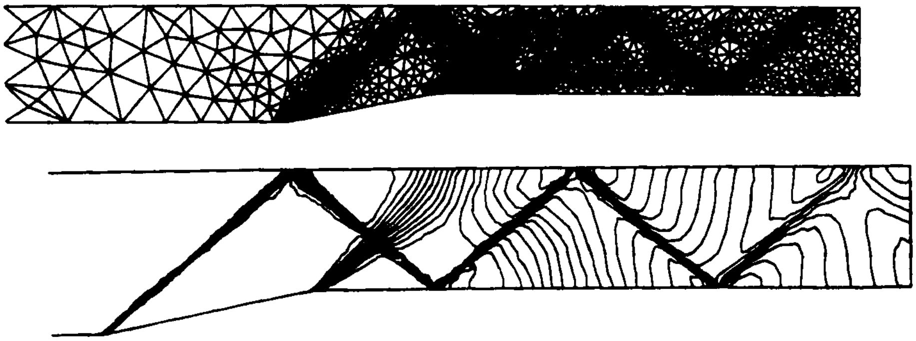

Figure 26. Third refined mesh and contours of density

three levels of refinement respectively. The mesh contains 943 mesh points with 115 points on the boundary after the first refinement. The number increases to 1576 mesh points with 129 points on the boundary after the second refinement and to 2285 mesh points with 136 points on the boundary after the third refinement. The improvement in the resolution of the flow after each refinement is apparent from the figures.

The theory of compressible flow gives an analytical solution for this flow, which makes it possible to compare the computational results with theoretical predictions. The necessary charts and tables required to determine the analytical solution are to be found in any text on compressible fluid dynamics (e.g. Reference 27). Figure 27 compares the contours of density shown in Figure 26 with the theoretically determined expansion and shock wave angles. As shown, the agreement between theory and computation is quite good.

The evaluation of the theoretical angles shown in the previous figure necessarily involves the determination of the Mach number as well. Thus the computed Mach number at various points in the flow field can also be compared with theoretical predictions. The unstructured mesh used makes it extremely difficult to obtain the distribution of Mach number along any cross-section of the channel. However, the Mach number distribution on the solid wall can be easily obtained. Figure 28 shows the variation in wall Mach number in the region of the upper wall where the oblique shock wave is reflected back into the flow. It is seen that the computed Mach number downstream of the reflection point is very close to the theoretical prediction. The computation

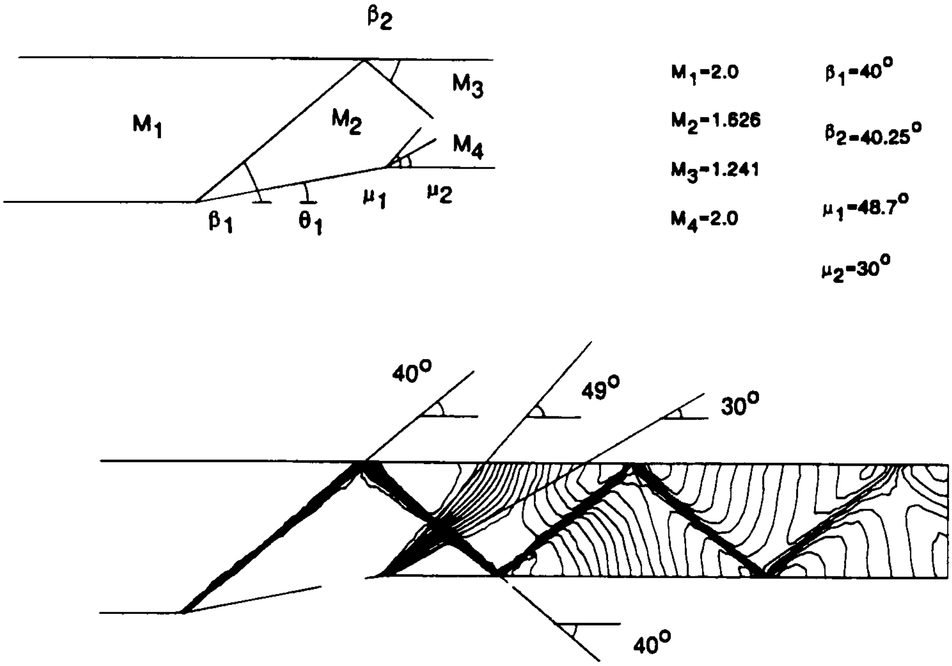

Figure 27. Comparison of theory and computational results

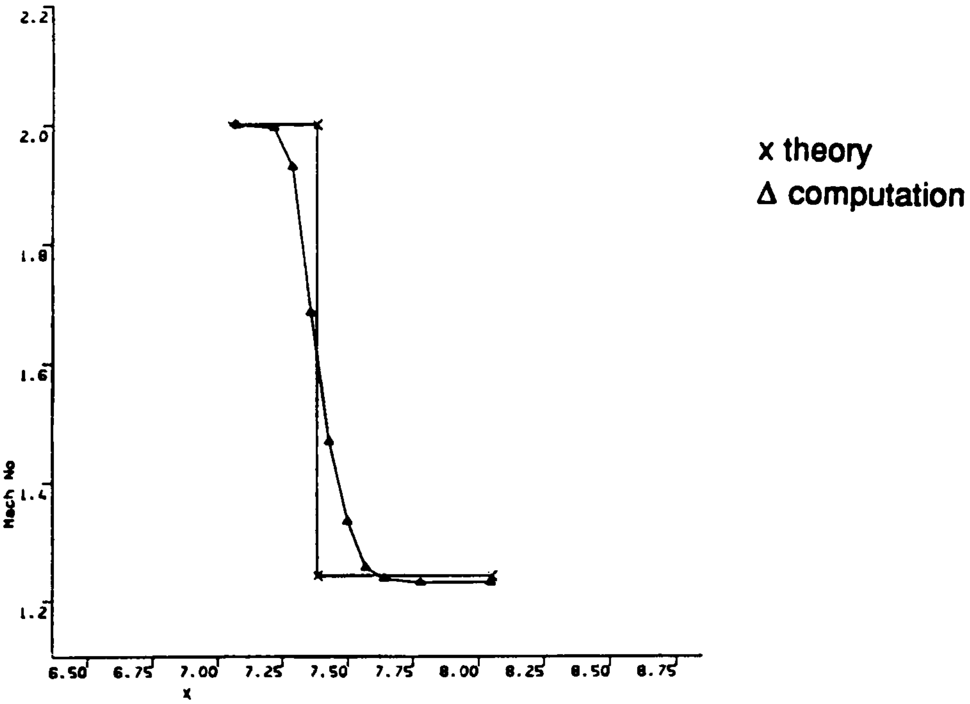

Figure 28. Mach number variation across shock reflection

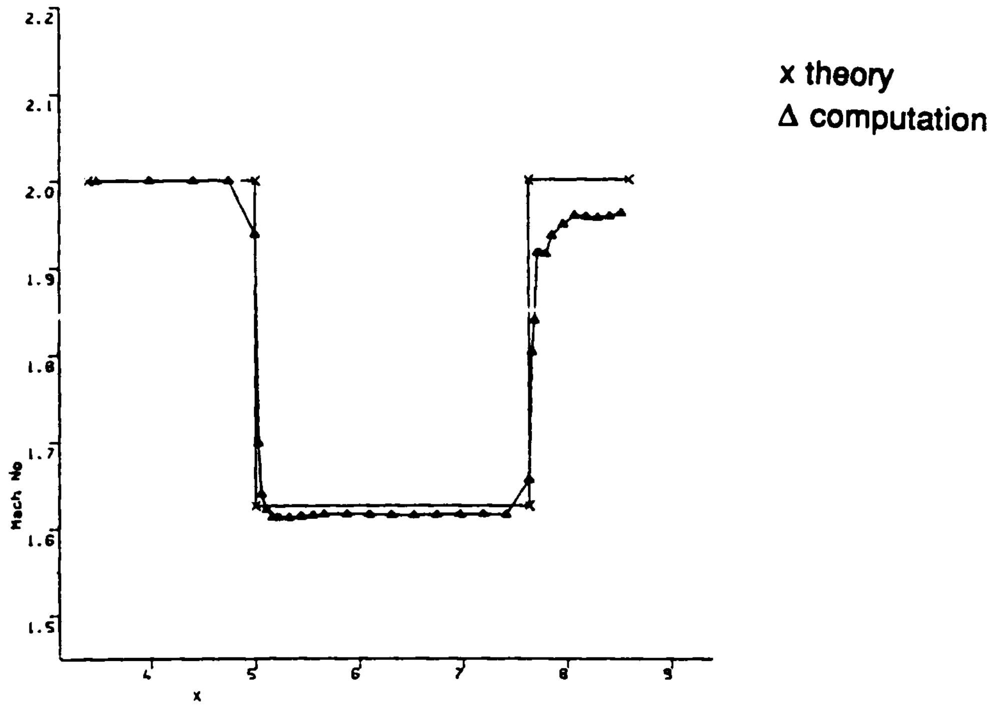

Figure 29. Mach number variation over ramp

also gives a relatively narrow region in which the Mach number varies from its upstream to its downstream value. Figure 29 shows the variation in wall Mach number along the lower wall from a point upstream of the foot of the ramp to a point downstream of the top of the ramp. Here the computed Mach number is seen to agree quite closely with the theoretical value, except in the region downstream of the expansion fan where there is a noticeable difference.

5. CONCLUSIONS

The KFVS finite volume scheme[16] has been extended for use with unstructured meshes. The algorithm has been applied to different geometries and over a range of Mach numbers. The incorporation of mesh adaptivity, using a local point enrichment method, substantially improves the quality of the solution. The results obtained using this scheme generally compare favourably with those obtained using a Jameson scheme. The importance of the high-resolution scheme has been clearly demonstrated for subsonic and transonic flow fields.

ACKNOWLEDGEMENTS

The authors wish to acknowledge the Procurement Executive of the Ministry of Defence through the Royal Aerospace Establishment, Farnborough, U.K. for providing the financial support for this work, and the National Aeronautical Laboratory, Bangalore, India for allowing one of the authors (J.S.M.) leave to work in Swansea. Particular thanks are expressed to Professor S. M. Deshpande and Dr. J. C. Mandal of the Indian Institute of Science, Bangalore for making available a version of the KFVS algorithm for structured grids.

REFERENCES

1. P. Eiseman, 'Grid generation for fluid mechanics computations', *Ann. Rev. Fluid Mech.*, **17,** 487–522 (1985).
2. J. F. Thompson, Z. U. A. Warsi and C. W. Mastin, *Numerical Grid Generation, Foundations + Applications*, North-Holland, Amsterdam, 1985.
3. N. P. Weatherill and C. R. Forsey, 'Grid generation and flow calculations for aircraft geometries', *J. Aircraft*, **22,** 855–860 (1985).
4. J. Peraire, J. Peiro, L. Formaggia, K. Morgan and O. C. Zienkiewicz, 'Finite element Euler computations in three dimensions', *AIAA Paper 88-0032*, 1988.
5. A. Jameson, T. J. Baker and N. P. Weatherill, 'Calculation of inviscid transonic flow over a complete aircraft', *AIAA Paper 86-0103*, 1986.
6. R. W. MacCormack and B. S. Baldwin, 'A numerical method for solving the Navier–Stokes equations with application to shock boundary layer interaction', *AIAA Paper 75-1*, 1975.
7. A. Jameson, W. Schmidt and E. Turkel, 'Numerical solution of the Euler equations by finite volume methods using Runge–Kutta time-stepping schemes', *AIAA Paper 81-1259*, 1981.
8. P. L. Roe, 'The use of the Riemann problem in finite-difference schemes', *Lecture Notes in Physics, Vol. 141*, Springer, Berlin, 1981, pp. 354–359.
9. P. L. Roe, 'Approximate Riemann solvers, parameter vectors and difference schemes', *J. Comput. Phys.*, **43,** 357 (1981).
10. S. Osher, 'Numerical solution of singular perturbation problems and hyperbolic systems of conservation laws', *North-Holland Mathematical Studies, Vol. 97*, North-Holland, Amsterdam, 1981, p. 179.
11. J. L. Steger and R. F. Warming, 'Flux vector splitting of the inviscid gasdynamic equations with application to finite difference methods', *J. Comput. Phys.*, **40,** 263 (1981).
12. B. Van Leer, 'Flux-vector splitting for the Euler equations', *Lecture Notes in Physics, Vol. 170*, Springer, Berlin, 1982, p. 507.
13. T. J. Barth and D. C. Jesperson, 'The design and application of upwind schemes on unstructured meshes', *AIAA Paper 89-0366*, 1989.
14. M. Vahdati, K. Morgan, J. Peraire and O. Hassan, 'A cell-vertex upwind unstructured grid solution procedure for high speed compressible viscous flow', in *Proc. Royal Aeronautical Society Int. Conf. on Hypersonic Aerodynamics*, Manchester, 12.1-12.22, 1989.
15. J. C. Mandal, 'Kinetic upwind method for inviscid compressible flows', *Ph.D. Thesis*, Indian Institute of Science, Bangalore, 1989.
16. J. C. Mandal and S. M. Deshpande, 'Higher order accurate kinetic flux vector splitting method for Euler equations', *Proc. Second Int. Conf. on Nonlinear Hyperbolic Problems*, Aachen, March 1988, *Notes on Numerical Fluid Mechanics, Vol. 24*, Vieweg, Braunschweig, 1989, pp. 384–392.
17. J. C. Mandal and S. M. Deshpande, 'Kinetic flux split upwind unsteady method with kinetic characteristic boundary conditions for Euler equations', *Fourth Natl Conf. on Aerodynamics*, Madras, December 1988.
18. J. C. Mandal and S. M. Deshpande, 'An upwind Euler space marching using kinetic flux vector splitting with new treatment of boundary conditions', *Fourth Asian Congr. of Fluid Mechanics*, Hong Kong, August 1989.
19. S. M. Deshpande, 'Kinetic theory based new upwind methods for inviscid compressible flows', *AIAA Paper 86-0275*, 1986.
20. S. M. Deshpande, 'A second order accurate kinetic theory based method for inviscid compressible flow', *NASA TP-2613*, 1986.
21. S. M. Deshpande, 'On the Maxwellian distribution, symmetric form, and entropy conservation for the Euler equations', *NASA TP-2583*, 1986.
22. N. P. Weatherill, 'The generation of unstructured grids using Dirichlet tessellations', *Department of Mechanical and Aerospace Engineering, Princeton University, Rep. 1715*, July 1985.
23. T. J. Baker, '3-dimensional mesh generation by triangulation of arbitrary point sets', *Proc. AIAA 8th Conf.*, Hawaii, June 1987, AIAA, New York, 1987.
24. N. P. Weatherill, 'The Delaunay triangulation in computational fluid dynamics', To appear *Comput. Math. Appl.*, (1992).
25. N. P. Weatherill, 'A method for generating irregular computational grids in multiply connected planar domains', *Int. j. numer. methods fluids*, **8,** 181–197 (1988).
26. N. P. Weatherill, *Grid Generation, VKI Lecture Series 1990-10*. Brussels, Belgium, June 1990.
27. H. W. Liepmann and A. Roshko, *Elements of Gasdynamics*, Wiley, New York, 1957.